Spatiotemporal Evolution of Runaway Electron Momentum Distributions in Tokamaks

Citation: Paz-Soldan, C.; Cooper, C.M.; Aleynikov, P.; Pace, D.C.; Eidietis, N.W. et al. "Spatiotemporal Evolution of Runaway Electron Momentum Distributions in Tokamaks." Physical Review Letters 118, 255002 (June 2017): 1- 6 © 2017 American Physical Society

As Published: http://dx.doi.org/10.1103/PhysRevLett.118.255002

Publisher: American Physical Society

Persistent URL: http://hdl.handle.net/1721.1/110251

Version: Final published version: final published article, as it appeared in a journal, conference proceedings, or other formally published context

Spatiotemporal Evolution of Runaway Electron Momentum Distributions in Tokamaks

C. Paz-Soldan,[1,*] C. M. Cooper,[2] P. Aleynikov,[3] D. C. Pace,[1] N. W. Eidietis,[1] D. P. Brennan,[4] R. S. Granetz,[5] E. M. Hollmann,[6] C. Liu,[4] A. Lvovskiy,[2] R. A. Moyer,[6] and D. Shiraki[7]
[1]*General Atomics, San Diego, California 92186, USA*
[2]*Oak Ridge Associated Universities, Oak Ridge, Tennessee 37831, USA*
[3]*Max-Planck Institute for Plasma Physics, Greifswald, Germany*
[4]*Princeton University, Princeton, New Jersey 05764, USA*
[5]*Massachusetts Institute of Technology, Cambridge, Massachusetts 02139, USA*
[6]*University of California–San Diego, La Jolla, California 92093, USA*
[7]*Oak Ridge National Laboratory, Oak Ridge, Tennessee 37831, USA*
(Received 31 January 2017; published 22 June 2017)

Novel spatial, temporal, and energetically resolved measurements of bremsstrahlung hard-x-ray (HXR) emission from runaway electron (RE) populations in tokamaks reveal nonmonotonic RE distribution functions whose properties depend on the interplay of electric field acceleration with collisional and synchrotron damping. Measurements are consistent with theoretical predictions of momentum-space attractors that accumulate runaway electrons. RE distribution functions are measured to shift to a higher energy when the synchrotron force is reduced by decreasing the toroidal magnetic field strength. Increasing the collisional damping by increasing the electron density (at a fixed magnetic and electric field) reduces the energy of the nonmonotonic feature and reduces the HXR growth rate at all energies. Higher-energy HXR growth rates extrapolate to zero at the expected threshold electric field for RE sustainment, while low-energy REs are anomalously lost. The compilation of HXR emission from different sight lines into the plasma yields energy and pitch-angle-resolved RE distributions and demonstrates increasing pitch-angle and radial gradients with energy.

DOI: 10.1103/PhysRevLett.118.255002

Introduction.—Reaching mega-ampere currents and mega-electron volt (MeV) energies during fast shutdown events, runaway electrons (REs) pose perhaps the greatest operational risk to tokamak fusion reactors such as ITER [1–4]. Because of the severe potential for damage to the reactor walls, opportunities for empirical tuning of RE control actuators will be limited. Instead, a first-principles predictive understanding is needed, and present-day experiments fill a crucial need in validating theoretical predictions of RE dissipation.

Classical theories for relativistic RE generation in tokamaks based on the effects of Coulomb collisions (small angle [5] and secondary avalanche [6]) determine the critical electric field (E_C) for the growth of RE populations. Further work highlighted the important role of synchrotron damping in elevating the threshold electric field above E_C [7,8], and several experiments have since yielded evidence of the elevated threshold [9–12]. These observations motivated the development of a rigorous analytical theory [13] and computational tools [14–19] that clarified the importance of the effects of pitch-angle scattering and synchrotron damping. Alongside quantifying the enhancement of the threshold field, these works predict phase-space circulation around an attractor resulting in a pileup of REs at specific energies potentially resulting in nonmonotonic features in the RE distribution function (f_e). While important to the RE dissipation rate and thus the prospects for control, neither have these features of f_e been directly observed nor has a detailed model validation of experimental f_e together with dissipation rates been made until now.

In this Letter, we report the first spatially, energetically, and temporally resolved reconstructions of f_e in tokamaks and their dependence on plasma parameters. The effect of varying synchrotron and collisional damping on f_e is directly shown, and direct comparisons to time-dependent modeling are made. This significantly expands on previous measurements [20–22] by spatially localizing the RE emission, isolating the synchrotron effect, and comparing directly to modeling. Experiments are conducted using trace RE populations in low-density Ohmic plasmas [11] in the DIII-D tokamak with parameters targeted to nondimensionally match the expected conditions in postdisruption RE beams in ITER, with both predicted to develop nonmonotonic f_e. Nonmonotonic features at the predicted energies are observed, and their dependence on synchrotron and collisional damping rates will be described.

Measurement technique.—Emission from RE populations are measured using a novel toroidally viewing (tangential) pinhole camera made entirely of lead, pictured in Fig. 1(a) and described in detail in Refs. [23,24]. Bremsstrahlung radiation emitted when a RE scatters off a plasma ion or neutral is collimated into the discrete sight lines of the camera. Because of the tangential view, only emission from low-pitch-angle REs is measured. The sight

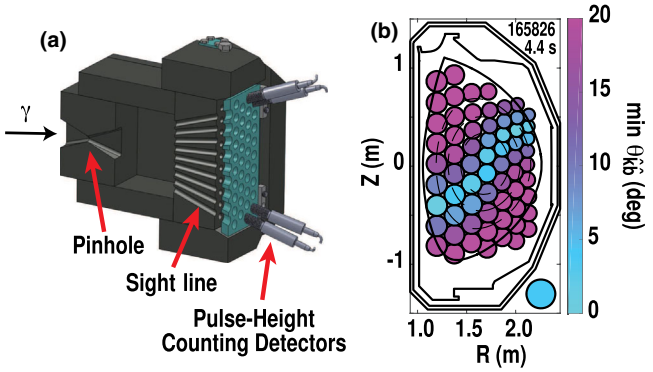

FIG. 1. (a) Lead pinhole camera geometry and (b) sight lines into the plasma at the tangency plane. Colors indicate the minimum angle ($\theta_{\hat{k}\hat{b}}$) between the magnetic field orientation ($\hat{b}$) and the sight-line orientation ($\hat{k}$). The lower-right circle in (b) denotes a full-view sight line.

lines view different parts of the plasma cross section, shown in Fig. 1(b). Along each sight line, different angles are made between the equilibrium magnetic field direction ($\hat{b}$, obtained from equilibrium reconstructions) and the sight-line orientation ($\hat{k}$). The minimum $\theta_{\hat{k}\hat{b}}$ along the sight line is used to color code the view. Emission along each active sight line is measured by a bismuth-germanate scintillating crystal together with a photodiode. The scintillation pulses from individual photons are digitized at a 10 MHz sample rate, with the pulse height determining the photon energy (E_γ). Binning the pulse heights in time allows an energy spectrum of hard-x-ray (HXR) photons (f_γ) to be assembled. f_γ is a convolution of f_e, the bremsstrahlung emission coefficients [25], and Compton scattering in the scintillator [26]. Assuming spatial homogeneity of f_e, knowledge of the bremsstrahlung emission and Compton scattering allows the inversion of f_γ to f_e by computing the expected f_γ from a set of monoenergetic f_e. In the inversions, finite pitch-angle effects are ignored; thus, only 1D experimental f_e are shown.

Background plasma and modeling framework.—The quiescent flattop scenario is employed [11]. The initial low-density operation builds a robust (and monotonic) RE population due to primary (Dreicer) production that also undergoes a secondary avalanche. When the REs reach a critical intensity, an asynchronous trigger at t_{puff} begins the RE dissipation phase. Here, background plasma properties such as the toroidal magnetic field (B_T) and the electron density (n_e) are actuated independently [shown in Fig. 2(a)] to vary the RE damping terms and study their effect on f_e. Primary production ceases in the dissipation phase as thermal transport changes reduce the electron temperature. Note that the dimensional B_T and n_e map to changes in the synchrotron and collisional damping terms and are nondimensionalized by the parameters $\hat{\tau}_r$ [$\equiv \frac{3}{2}(m_e \ln\Lambda/\epsilon_0)\times(n_e/B_T^2) \approx 28\{n_e[10^{19}\text{m}^{-3}]/(B_T[\text{T}])^2\}$, the ratio of the collision to the synchrotron damping time] and E/E_C

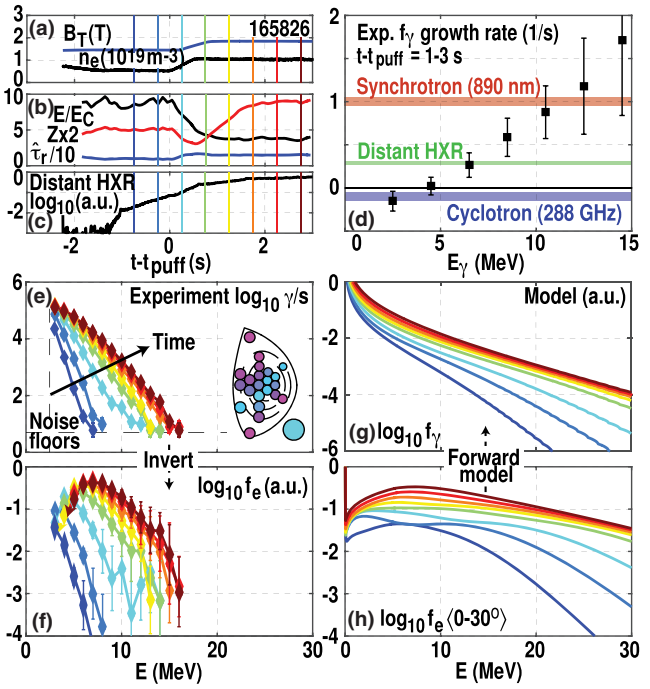

FIG. 2. (a) Experimental actuators, (b) nondimensional parameters, and (c) distant HXR signal for a typical discharge. (d),(e) Measured f_γ shows an increasing growth rate as the energy increases and flattening at midenergy consistent with (f) nonmonotonic f_e feature formation. (g),(h) Model predictions of f_γ and f_e are broadly consistent with the data.

($\equiv(4\pi\epsilon_0^2 m_e V_C^2/n_e e^3 \ln\Lambda) \approx 10\{V_{\text{loop}}[\text{V}]/n_e[10^{19}\text{m}^{-3}]\}$, the ratio of the toroidal electric field to the critical field). E is measured at the plasma surface, but any radial gradients relax quickly (< 1 s) compared to discharge time scales. The ion charge Z is also measured with charge exchange spectroscopy and actuated by replacing deuterium ions ($Z = 1$) with nitrogen ions ($Z = 7$) holding n_e constant. The plasma retains keV thermal temperatures and is thus fully ionized, so no corrections due to bound electrons are needed. The nondimensional E/E_C, Z, and $\hat{\tau}_r$ accessed are similar to expected values in ITER, thus giving access to ITER-relevant RE dissipation regimes.

To model the evolution of f_e, the time-dependent relativistic 2D Fokker-Planck equation (for example, Ref. [27]) is solved numerically inputting measured on-axis (spatially 0D) plasma parameters [Fig. 2(b)]. The equation as in Ref. [13] is solved with two amendments: (i) The collision operator is extended to be valid for lower energies (similar to Refs. [28,29]), and (ii) an approximate secondary source is included which captures the effect of a finite energy incident electron population. This treatment accurately captures the analytical results of RE generation models [5,6,30] as well as the near-threshold regime [13]. The computed f_e evolution is then placed through a forward model taking into account bremsstrahlung emission coefficients and sight-line geometry to obtain the

predicted f_γ [24]. Unlike inversion from f_γ to f_e, forward modeling from f_e to f_γ requires no assumptions, though in accordance with the tangential view only the low-pitch-angle part of the distribution $\langle 0°–30° \rangle$ is used in the f_γ calculation (though taken to have zero pitch angle).

Global distribution measurement.—The discharge in Fig. 2 accesses strong synchrotron damping ($\hat{\tau}_r \approx 15$), high Z (≈ 4), and modest collisional damping ($E/E_C \approx 4$) [Figs. 2(a) and 2(b)]. For these parameters, the total HXR energy flux measured on a distant plastic scintillator [Bicron BC-400, Fig. 2(c)] grows. Measurements (here aggregating all spatial channels) find very different f_γ growth rates with HXR energy (E_γ) [Fig. 2(d)]. Comparisons of growth rates across emission bands are consistent. At low E_γ (≤ 2 MeV), f_γ decays together with 288 GHz electron cyclotron emission (ECE), as expected, since ECE is dominated by low-energy REs. Similarly, high E_γ growth rates match that of visible synchrotron emission (SE) at 890 nm, as expected, since SE is dominated by high-energy (> 10 MeV) REs [31]. The growth rate of the distant HXR detector is skewed to low E_γ, indicating that this type of diagnostic (often used to infer RE population) does not clearly discriminate between RE energy and population.

Measurements of f_γ and inversion to f_e [Figs. 2(e) and 2(f)] reveal f_γ changes at midenergy which upon inversion map to the development of a nonmonotonic f_e from an originally peaked f_e. Modeling of this same discharge to predict f_e and forward model f_γ [Figs. 2(g) and 2(h)] indicates a similar evolution is predicted. As with the experiment, f_γ increases more rapidly at high energy, and a nonmonotonic feature in f_e is computed for these experimental conditions at a similar energy (≈ 7 MeV). The final f_e shape is near stationary, indicating the phase-space circulation effect gives rise to the nonmonotonic feature. Note that the absence of f_e points late in time below 5 MeV is due to the prediction of slightly negative f_e (with a large uncertainty) due to the subtractions involved in the inversion process, indicating that, while the degree of hollowness is difficult to quantify, peaked f_e are excluded. Additionally, two experimental noise floors are present: at low flux due to limited counting statistics ($\leq 5\gamma/$ s) and at low energy due to pulse heights approaching electronic noise levels (≤ 1 MeV). Modeled f_e are momentum-space distributions plotted against energy, normalized by $n_{\mathrm{RE}} = \int f_e dp$, and take units [$\gamma$/MeVs]. While normalization affects the f_e shape, this normalization follows directly from the experiment (γ/s count rate histograms with uniform 1 MeV binning) and also highlights attractor dynamics.

Angular and spatial dependencies.—Comparison of f_γ from individual sight lines allows the extraction of radial and pitch-angle profiles of sufficiently energetic REs. This is due to the angular localization of bremsstrahlung emission provided by the relativistic forward-beaming effect. Assuming f_e decreases with the pitch

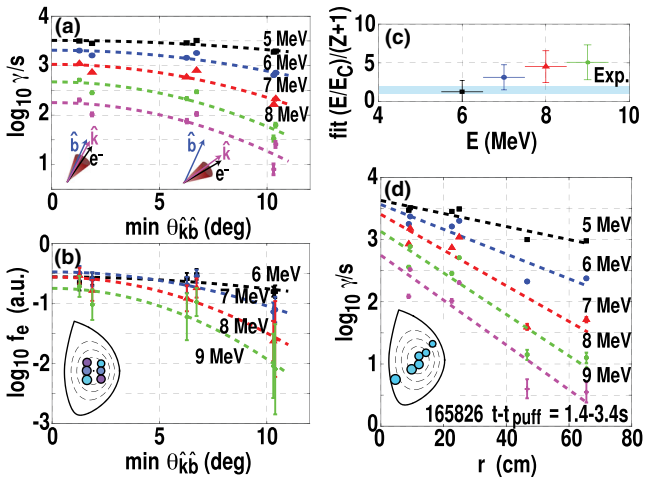

FIG. 3. Angular and spatial RE distribution dependency for the same discharge of Fig. 2. Experimental (a),(b) f_γ and f_e show reductions at high $\theta_{\hat{k}\hat{b}}$, allowing (c) the inference of E/E_C to $(Z+1)$ according to Ref. [13]. (d) Energy-dependent f_γ radial falloff is also observed.

angle, emission into a sight line with a small minimum $\theta_{\hat{k}\hat{b}}$ will be dominated by small-pitch-angle REs. In contrast, emission into sight lines with large minimum $\theta_{\hat{k}\hat{b}}$ will predominantly see REs whose pitch angle roughly matches $\theta_{\hat{k}\hat{b}}$. Contributions from larger $\theta_{\hat{k}\hat{b}}$ points along any sight line are weaker as f_e (and thus emission) decreases with the pitch angle. Measurement geometry is further described in Ref. [24]. Thus, comparing f_γ from sight lines viewing the same flux surface at different minimum $\theta_{\hat{k}\hat{b}}$ is roughly equivalent to resolving the f_γ pitch-angle distribution. An example pitch-angle-resolved f_γ measurement is shown in Fig. 3(a), plotting against the minimum $\theta_{\hat{k}\hat{b}}$ and illustrating energy-dependent falloff. Note that 10 MeV emission cones are narrower than minimum $\theta_{\hat{k}\hat{b}}$ separation (see the cartoon), though blurring does occur below 5 MeV, setting a low E_γ angular resolution limit. f_γ from each sight line can be inverted [Fig. 3(b)], confirming expectations of a more forward beamed f_e at higher energy. The inferred f_e pitch-angle dependence can be compared to theoretical predictions [13] of exponential angle falloff with a decay coefficient proportional to the ratio of E/E_C to $Z+1$. As shown in Fig. 3(c), the prediction is within the experimental uncertainty below 7 MeV. At higher energy, f_e is more forward beamed than expected for reasons that are not yet understood, though uncertainties are larger for this measurement due to the lower counting statistics of single sight lines. Improving counting statistics through repeat discharges or increased detector efficiency will reduce uncertainty at high E_γ, allowing, for example, the formulation of Ref. [8] to be validated. Future work will also pursue 2D (angle-resolved) f_e inversions.

Individual sight lines with the same low minimum $\theta_{\hat{k}\hat{b}}$ but viewing different flux surfaces can also be used to

measure radial profiles of f_γ, as shown in Fig. 3(d). As with the pitch-angle distribution, radial falloff is more pronounced at high energy, indicating that energy-dependent spatial transport is present.

Global parametric dependencies.—Modifying the synchrotron and collisional damping rate is found to have a strong effect on the measured f_γ and f_e in both the theory and the experiment (aggregating now over all active sight lines). The effect of synchrotron radiation is isolated by using three matched discharges with similar prehistories and postpuff parameters ($E/E_C = 3.1 \pm 0.3$ and $Z = 1.4 \pm 0.1$) but varying B_T, thus accessing a wide range of $\hat{\tau}_r$ [Figs. 4(a) and 4(b)]. Experimental f_γ [Fig. 4(c)] demonstrate a reduction in high E_γ counts and an increased spectral index as B_T is raised, opposite to the expectation from single-particle confinement arguments yet consistent with synchrotron effects limiting the high-energy f_e. Interestingly, at low E_γ a decrease in f_γ is found with decreasing B_T. Experimental f_e [Fig. 4(d)] indicates that the RE distribution is getting progressively flatter as B_T is decreased, with the lowest B_T displaying a nonmonotonic feature in f_e outside of the experimental uncertainty. Modeling of these cases [Figs. 4(e) and 4(f)] qualitatively predicts the observed shape variations with $\hat{\tau}_r$. However, variations between f_e and f_γ at different $\hat{\tau}_r$ are observed at a lower energy than in modeling, indicating a stronger B_T effect in the experiment potentially due to the neglect of spatial effects. Indeed, the input on-axis B_T value is lower than the inboard value, which is also where visible synchrotron emission is known to be localized [11,31].

Considering emission growth rates [Figs. 4(g) and 4(h)], the distant HXR, ECE, and low E_γ f_γ growth rates all decrease with increasing B_T. In contrast, SE and high E_γ f_γ rates display the opposite B_T trend. All emissions are thus broadly consistent a shift to a high energy as B_T is lowered. Note, however, that quantitative ECE and SE growth rates differ from the f_γ rates, due to the direct B_T dependencies of these emissions. The corresponding model-predicted f_γ growth rates are shown in Fig. 4(i). Agreement is good at high E_γ, though at low E_γ the observed decay is not reproduced unless the secondary source term is artificially removed as might be expected if E/E_C were somewhat lower.

Increasing collisional damping by raising n_e and thus decreasing E/E_C [Figs. 5(a) and 5(b)] is found to decrease the growth rate of HXR emission [Fig. 5(c)] across all E_γ. Growth rates of all other measured emissions (ECE, SE, distant HXR) also decrease as E/E_C is reduced (not shown). A transition from HXR signal growth to decay at E/E_C far above $E/E_C = 1$ is measured on the distant plastic scintillator (as reported in Refs. [11,12]), but the E_γ

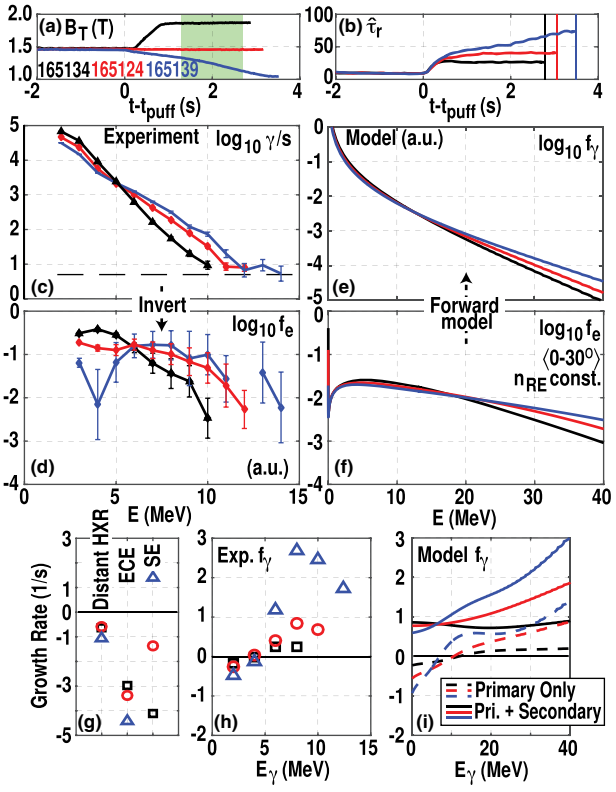

FIG. 4. Effect of modifying synchrotron force on RE distributions actuated through (a) varying the toroidal field (B_T) resulting in a wide change in $\hat{\tau}_r$ (b). Measured (c) f_γ and (d) f_e from the green interval in (a) show an expansion to a high energy and contraction at a low energy. Model (e) f_γ and (f) f_e show qualitative similarity (note the different energy scale), normalizing to constant n_{RE}. Growth rate analyses for (g) other diagnostics, (h) experimental f_γ, and (i) model f_γ are also shown.

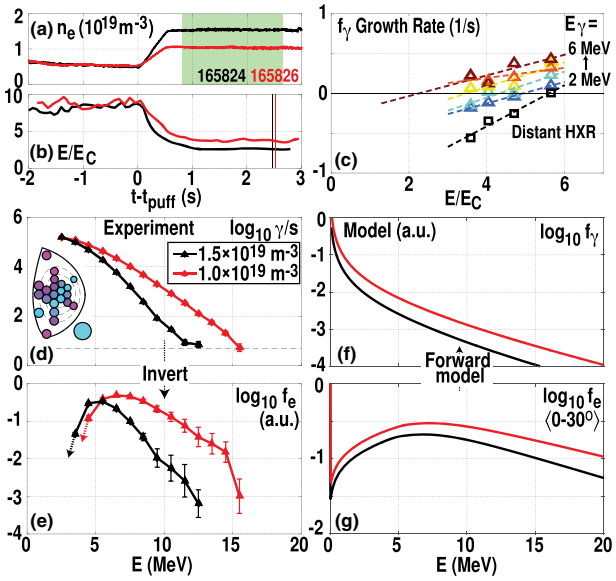

FIG. 5. Effect of modifying collisional damping by increasing (a) n_e resulting in (b) a decrease in E/E_C. Measured (c) f_γ and (d) f_e from the green interval in (a) indicate that RE energization is inhibited, consistent with model-predicted (e) f_γ and (f) f_e. (g) f_γ growth rates indicate that high-energy REs decay at a lower E/E_C than low-energy REs.

dependence of this diagnostic is unclear. E_γ-resolved measurements reveal an increasing HXR growth rate with E_γ at fixed E/E_C [also seen in Fig. 4(h)]. Thus, the E/E_C value where HXR growth transitions to decay decreases with increasing E_γ. While an extrapolation is necessary to find this value at a high energy, it is roughly at $E/E_C \approx 2$. This compares more favorably to the threshold field for RE generation which is predicted to be at $E/E_C = 1.6$ for these conditions [13], indicating a more consistent behavior at high energy. Comparison of experimental and model f_γ and f_e [Figs. 5(d)–5(g)] shows good agreement, with the high E/E_C case extending to higher energy and with a harder spectral index than at low E/E_C. The experimental nonmonotonic feature increases in energy from 5 to 7 MeV as E/E_C is raised, also in good agreement with model predictions (from 6 to 7 MeV).

Summary and conclusion.—Comparing experimental and modeled f_e, nearly all qualitative trends are captured: (i) Both develop nonmonotonic features at consistent energy, (ii) f_e are more parallel directed at a high energy, (iii) increasing synchrotron damping (lowering $\hat{\tau}_r$) shifts f_e towards a lower energy, and (iv) increasing collisional damping (lowering E/E_C) decreases f_e at all energies. The f_e shape and location of nonmonotonic features are generally in agreement as E/E_C and $\hat{\tau}_r$ are varied.

An exception to the wide qualitative agreement between the experiment and theory is the behavior at low energy, where systematically lower f_γ growth rates are observed. The cause remains unknown but may be due to spatial transport effects not included in the 0D model [32]. Allowing for momentum-dependent spatial diffusion (as expected from magnetic fluctuations) also introduces free parameters to fit the observed spatial f_e trends but does not exclude other mechanisms (such as kinetic instability due to the f_e shape) from impacting the spatial gradients. Other spatial effects, such as an increase of the calculated synchrotron damping under a full-orbit treatment [33], may also contribute to explaining the quantitatively stronger effect of B_T seen in the experiment.

In conclusion, novel measurements provide the first confirmation of nonmonotonic features in RE distribution functions and their dependence on collisional and synchrotron damping terms. The broad agreement found validates the importance of these effects and improves confidence that these models can be used to design optimized RE mitigation strategies. Looking forward, the identified discrepancies will guide improvements to RE dissipation models and enable improved validation against the spatial, temporal, pitch-angle, and energetic effects described herein.

DIII-D data shown in this Letter can be obtained in digital format by following the links at Ref. [34].

The authors thank M. Austin, S. Haskey, B. Grierson, J. Kulchar, D. Taussig, and Y. Zhu for diagnostic support, as well as N. Commaux and A. Wingen for their assistance, and T. Fülöp, O. Embréus, A. Stahl, and G. Wilkie for useful discussions. This material is based upon work supported in part by the U.S. Department of Energy under Grants No. DE-FC02-04ER54698, No. DE-FG02-07ER54917, No. DE-AC05-00OR22725, No. DE-FC02-99ER54512, and No. DE-SC0016268.

*paz-soldan@fusion.gat.com

[1] T. C. Hender *et al.*, Nucl. Fusion **47**, S128 (2007).
[2] M. Lehnen *et al.*, J. Nucl. Mater. **463**, 39 (2015).
[3] E. M. Hollmann *et al.*, Phys. Plasmas **22**, 021802 (2015).
[4] A. H. Boozer, Phys. Plasmas **22**, 032504 (2015).
[5] J. Connor and R. Hastie, Nucl. Fusion **15**, 415 (1975).
[6] M. N. Rosenbluth and S. V. Putvinski, Nucl. Fusion **37**, 1355 (1997).
[7] J. R. Martin-Solis, J. D. Alvarez, R. Sanchez, and B. Esposito, Phys. Plasmas **5**, 2370 (1998).
[8] F. Andersson, P. Helander, and L. G. Eriksson, Phys. Plasmas **8**, 5221 (2001).
[9] J. R. Martin-Solis, R. Sánchez, and B. Esposito, Phys. Rev. Lett. **105**, 185002 (2010).
[10] E. M. Hollmann *et al.*, Nucl. Fusion **51**, 103026 (2011).
[11] C. Paz-Soldan, N. W. Eidietis, R. S. Granetz, E. M. Hollmann, R. A. Moyer, N. A. Crocker, A. Wingen, and Y. Zhu, Phys. Plasmas **21**, 022514 (2014).
[12] R. S. Granetz, B. Esposito, J. H. Kim, R. Koslowski, M. Lehnen, J. R. Martin-Solis, C. Paz-Soldan, T. Rhee, J. C. Wesley, L. Zeng, and (the ITPA MHD Group), Phys. Plasmas **21**, 072506 (2014).
[13] P. B. Aleynikov and B. N. Breizman, Phys. Rev. Lett. **114**, 155001 (2015).
[14] P. B. Aleynikov, K. Aleynikova, B. N. Breizman, G. T. A. Huijsmans, S. V. Konovalov, S. V. Putvinski, and V. Zhogolev, in *Proceedings of the 25th IAEA Fusion Energy Conference, St. Petersburg, Russian Federation* (2014), p. TH/P3–38.
[15] E. Hirvijoki, I. Pusztai, J. Decker, O. Embréus, A. Stahl, and T. Fülöp, J. Plasma Phys. **81**, 475810502 (2015).
[16] A. Stahl, E. Hirvijoki, J. Decker, O. Embréus, and T. Fülöp, Phys. Rev. Lett. **114**, 115002 (2015).
[17] C. Liu, D. P. Brennan, A. H. Boozer, and A. Bhattacharjee, Phys. Plasmas **23**, 010702 (2016).
[18] J. Decker, E. Hirvijoki, O. Embréus, Y. Peysson, A. Stahl, I. Pusztai, and T. Fülöp, Plasma Phys. Controlled Fusion **58**, 025016 (2016).
[19] C. Liu, D. P. Brennan, A. H. Boozer, and A. Bhattacharjee, Plasma Phys. Controlled Fusion **59**, 024003 (2017).
[20] A. E. Shevelev, E. M. Khilkevitch, V. G. Kiptily, I. N. Chugunov, D. B. Gin, D. N. Doinikov, V. O. Naidenov, A. E. Litvinov, and I. A. Polunovskii, Nucl. Fusion **53**, 123004 (2013).
[21] A. E. Shevelev, E. M. Khilkevitch, S. I. Lashkul, V. V. Rozhdestvensky, and A. B. Altukhov, Nucl. Instrum. Methods Phys. Res., Sect. A **830**, 102 (2016).
[22] E. M. Hollmann, P. B. Parks, N. Commaux, N. W. Eidietis, R. A. Moyer, D. Shiraki, M. E. Austin, C. J. Lasnier, C.

Paz-Soldan, and D. L. Rudakov, Phys. Plasmas **22**, 056108 (2015).
[23] D. C. Pace, C. M. Cooper, D. Taussig, N. W. Eidietis, E. M. Hollmann, V. Riso, and M. A. Van Zeeland, Rev. Sci. Instrum. **87**, 043507 (2016).
[24] C. M. Cooper, D. C. Pace, N. Commaux, N. W. Eidietis, E. M. Hollmann, and D. Shiraki, Rev. Sci. Instrum. **87**, 11E602 (2016).
[25] H. W. Koch and J. W. Motz, Rev. Mod. Phys. **31**, 920 (1959).
[26] Y. Peysson and F. Imbeaux, Rev. Sci. Instrum. **70**, 3987 (1999).
[27] L.-G. Eriksson and P. Helander, Comput. Phys. Commun. **154**, 175 (2003).
[28] P. Helander, *Collisional Transport in Magnetized Plasmas* (Cambridge University, Cambridge, England, 2002).
[29] G. Papp, M. Drevlak, T. Fülöp, and P. Helander, Nucl. Fusion **51**, 043004 (2011).
[30] P. B. Parks, M. Rosenbluth, and S. Putvinski, Phys. Plasmas **6**, 2523 (1999).
[31] J. H. Yu, E. M. Hollmann, N. Commaux, N. W. Eidietis, D. A. Humphreys, A. N. James, T. C. Jernigan, and R. A. Moyer, Phys. Plasmas **20**, 042113 (2013).
[32] P. Helander, L.-G. Eriksson, and F. Andersson, Phys. Plasmas **7**, 4106 (2000).
[33] L. Carbajal, D. Del-Castillo-Negrete, D. Spong, S. Seal, and L. Baylor, Phys. Plasmas **24**, 042512 (2017).
[34] https://fusion.gat.com/global/D3D_DMP.